

Supporting Information

Cutting “lab-to fab” short: High Throughput Optimization and Process Assessment in Roll-to-Roll Slot Die Coating of Printed Photovoltaics

Michael Wagner^{1,2}, Andreas Distler², Vincent M. Le Corre², Simon Zapf², Burak Baydar², Hans-Dieter Schmidt², Madeleine Heyder², Karen Forberich^{1,2}, Larry Lürer^{1,2}, Christoph J. Brabec^{1,2}, H.-J. Egelhaaf^{1,2}

¹*Forschungszentrum Jülich GmbH, Helmholtz-Institute Erlangen-Nürnberg for Renewable Energy (HI ERN), Dept. of High Throughput Methods in Photovoltaics, Erlangen, Germany*

²*Friedrich-Alexander-Universität Erlangen-Nürnberg, Materials for Electronics and Energy Technology (i-MEET), Erlangen, Germany*

1. Spectral Data Processing and Analysis:

Due to inhomogeneities in the active layer (slightly fluctuating thickness) and the movement of the web (slight variance of web position and tilt with respect to the spectrometer beam), the spectral raw data has a noisy appearance. However, the majority of this “noise” is systematic and identical for all wavelengths, as can be seen in Figure S1 (grey curves). Consequently, the temporal evolution of the absorption at the isosbestic point (~600 nm), i.e., the wavelength at which the absorbance should – in theory – stay constant over time, can be used to correct/smoothen the signals at all other wavelengths using Equation S1.

$$A_{corrected}(\lambda, t_x) = \frac{A_{raw}(\lambda, t_x)}{A_{isosbestic}(t_x)} * \bar{A}_{isosbestic} \quad \text{Eq. S1}$$

Here, $A_{raw}(\lambda, t_x)$ is the absorbance at a certain wavelength and a certain point in time, $A_{isosbestic}(t_x)$ the respective absorbance at the isosbestic point, and $\bar{A}_{isosbestic}$ the average absorbance over all times at the isosbestic wavelength. The resulting processed data is also plotted in Figure S1 (colored curves).

The respective mass fractions of the donor and acceptor are calculated from the spectral data according to Equation S2 and Equation S3.

$$w_D(t_x) = \frac{A_{corrected}(517 \text{ nm}, t_x) - A_{corrected}(517 \text{ nm}, t_0)}{A_{corrected}(517 \text{ nm}, t_{end}) - A_{corrected}(517 \text{ nm}, t_0)} \quad \text{Eq. S2}$$

$$w_A(t_x) = 1 - w_D(t_x) \quad \text{Eq. S3}$$

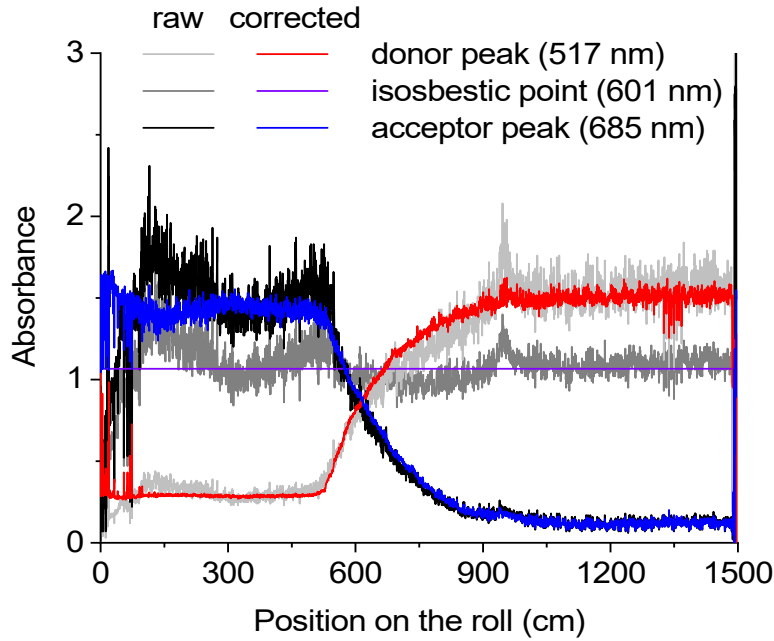


Figure S1: Temporal evolution of the spectral raw data (grey/black) and the data processed according to Eq. S1 (colored) for three different wavelengths.

2. Determination of dry film thickness:

The dry film thickness of the SnO₂ variation is calculated with the following formula, where we assumed that the space filling of SnO₂ nanoparticles is 0.74. The bulk densities of SnO₂ and Butanol are 6.95 g/cm³ and 0.81 g/cm³, respectively. This calculation gives a rough estimate of the final dry film thickness.

$$\text{Dry film thickness} = \frac{\text{Flowrate}}{\text{Web speed} \times \text{Coating width}} \times \frac{\text{Conc}(w/w) \times \rho_{\text{BuOH}}}{\rho_{\text{SnO}_2} \times \text{packing density}} \quad \text{Eq.}$$

3. Experimental Design:

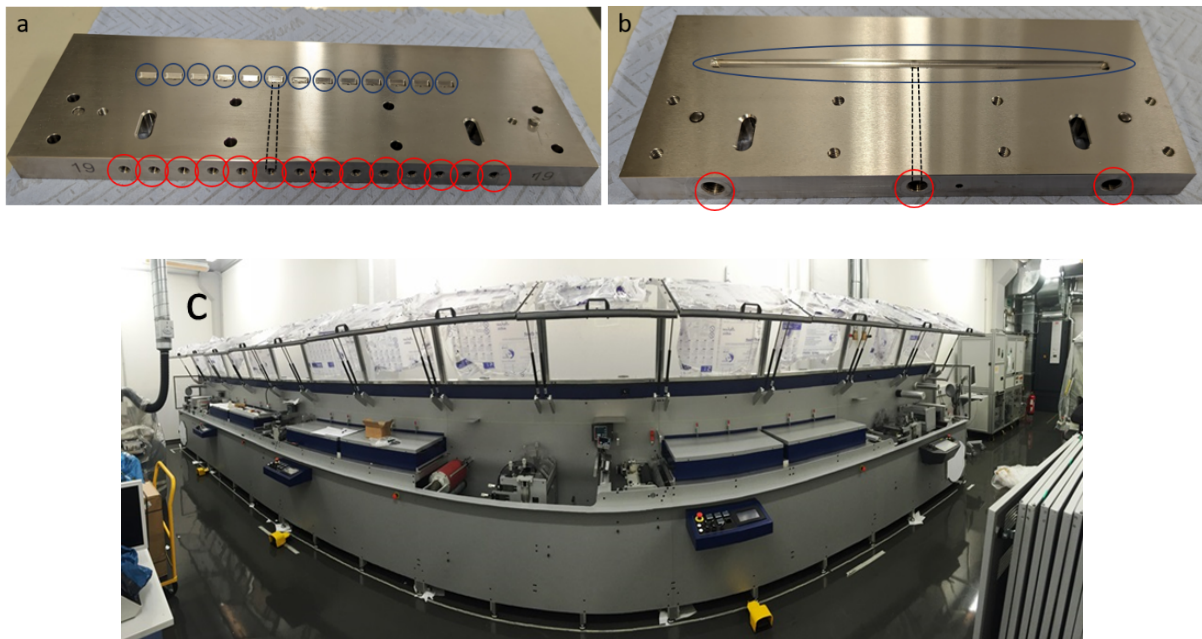


Figure S2: (a) Multi Channel Slot Die with 13 reservoirs (blue circles) and 14 individual inlets (red circles, the one on the far right is not connected to a reservoir) , which is used for active layer, HTL and Ag NW coating. On each photograph, one of the channels which connect inlets to reservoirs is marked exemplarily with black dashed lines. (c) full view of the roll-to-roll coating machine.

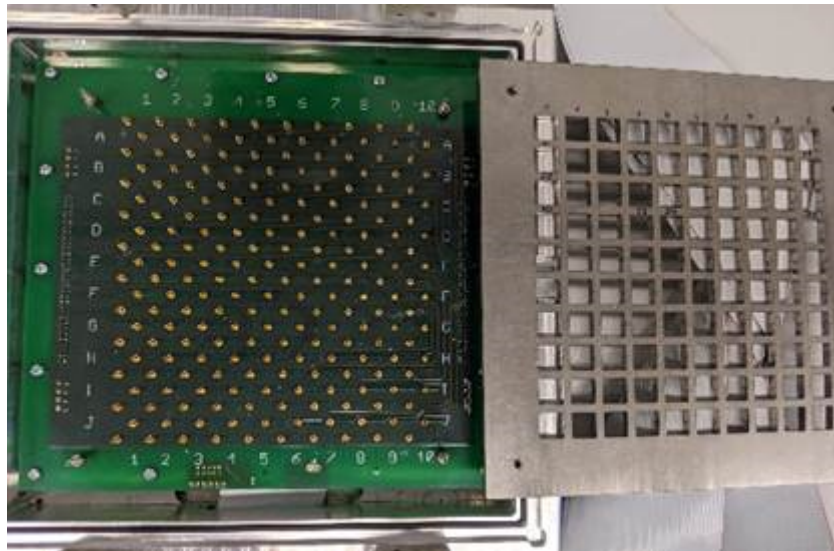
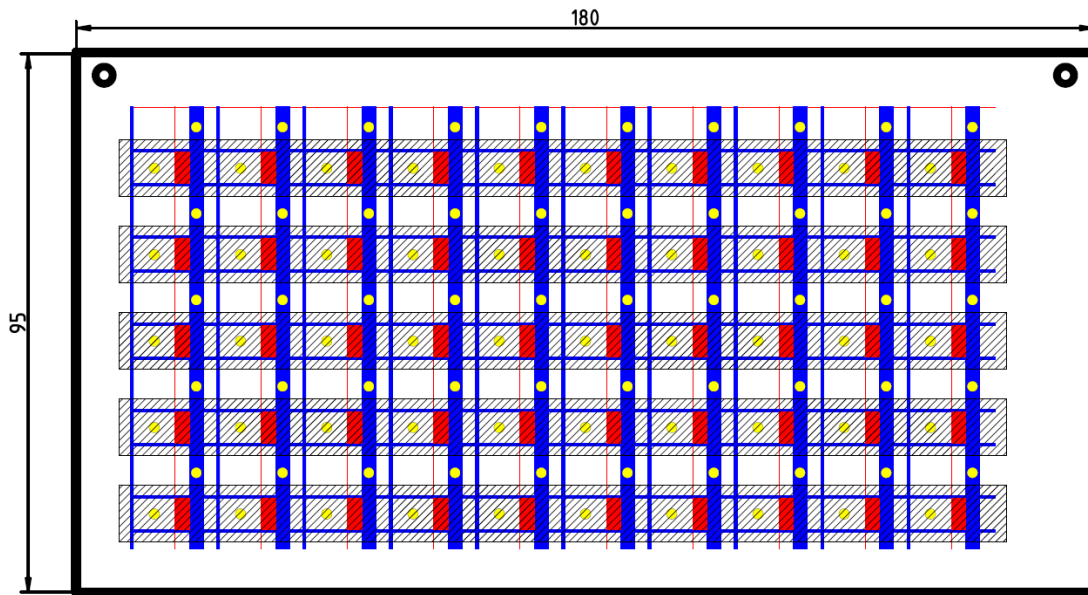


Figure S3: Top: Schematic of the measured sheets, where the red lines mark the P1 lines (removal of bottom electrode), the blue lines the removal of the top electrode, the red boxes the active area of the solar cells, the dashed lines the five different SnO₂ stripes, the yellow circles the contact spots of the top and bottom electrode and the black circles the alignment holes. Bottom: Measurement board that was specifically designed and built to measure these sheets. After mounting the sheets, the measurement board is covered with a glass plate (not shown here), sealed, and flooded with nitrogen for 30 s before exposing it to the solar simulator.

4. Comparison of solar cell parameters with results obtained by blade-coating on single substrates

In Figure S4, we present experimental data for D:A variation that we obtained by blade coating on separate substrates, with PCE, FF, Voc, Jsc, injection current (extracted from the light curve at +1.2 V) and leakage current (extracted from the dark curve at -0.5 V) given in the separate panels. The layer stack is the same as used in the R2R experiment (PET/IMI/SnO2/P3HT:oIDTBR/PEDOT:PSS/AgNW). The SnO2 thickness was 23 nm and the D:A ratio was varied as 2:1, 1.5:1, 1:1, 1:1.5, and 1:2. Figure 2 shows that the highest efficiency is achieved for a D:A ratio of 1:1.5, due to the highest Jsc for all the ratios that were tried. This value and also the general parameter dependence are consistent with the optimum ratio of 1.44 obtained from the high throughput experiment.

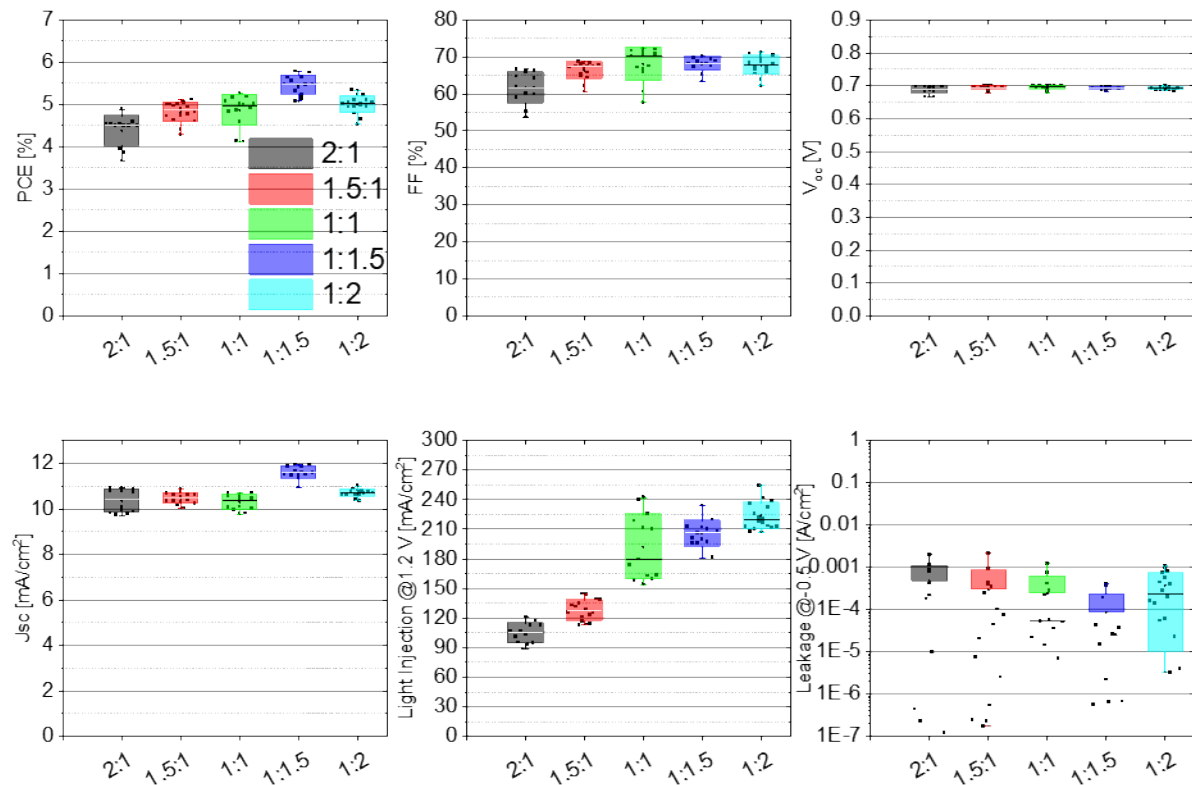


Figure S4: Performance parameters obtained from the D:A ratio variation with P3HT:o-IDTBR by manual blade coating on single substrates.

In Figure S5, we present analogous experimental data for SnO₂ layer thickness variation and D:A ratio of 1:1. The layer thickness variation is achieved by varying the coating speed and the concentration of the SnO₂ solution. The determination of layer thickness is not as

straightforward as for the R2R experiment. Instead of calculating it from the used volume of the ink and the concentration, layer thicknesses were calibrated by measuring several films with a profilometer (shown in Figure S6). The accuracy of this measurement is limited by the thickness variation that can occur on the small substrate.

In the manual experiment, variation 6 with an approximate layer thickness of 11.5 nm exhibits the best efficiency value. This is consistent with the results in the main manuscript, where the variation with 12.1 nm thickness gives the best efficiency. Whereas there are further trends that are the same in both automated and manual experiment (a pronounced drop in V_{oc} for SnO_2 thicknesses below ~ 10 nm, or a pronounced drop in J_{sc} for thicknesses of ~ 100 nm), other trends cannot be exactly reproduced (for instance, the automated experiment shows a clear optimum at 12.1 nm, whereas the in manual experiment variations 2,3,4,5 are very similar within the statistical variation).

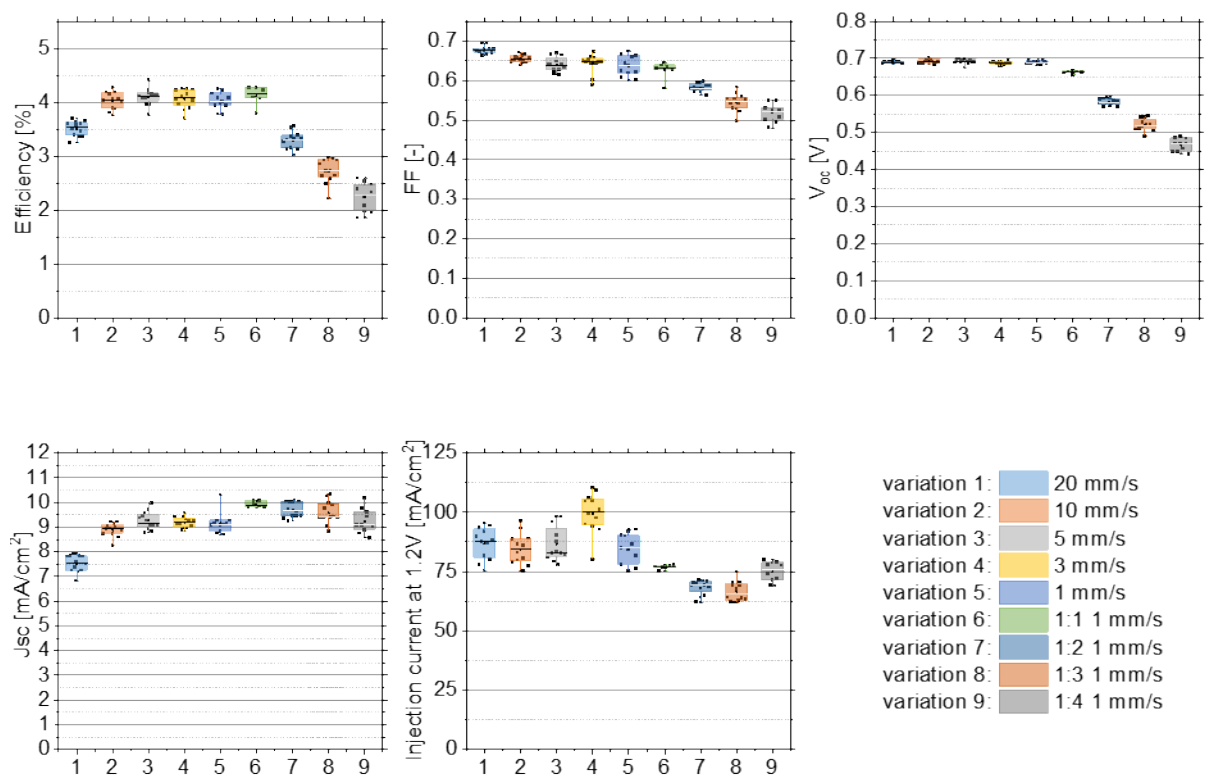


Figure S5: Performance parameters obtained from the variation of the SnO₂ layer thickness by manual blade coating on single substrates (D:A ratio 1:1).

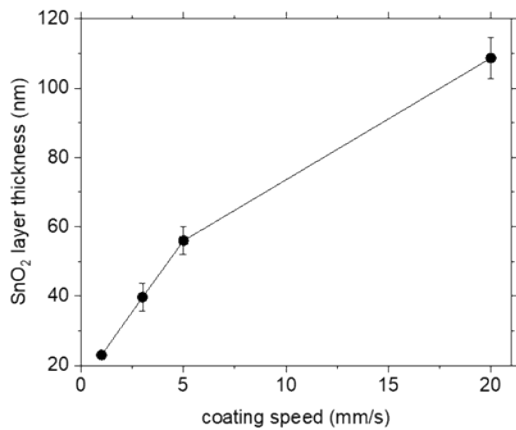


Figure S6: Calibration of SnO₂ Layer thickness obtained from profilometer measurements. Left: measured values, right: interpolation for the coating speeds used for the data shown in Figure 3. For variations 6 – 9, thickness values were calculated under the assumption that the thickness is inversely proportional to the dilution.

5. GPR Analysis

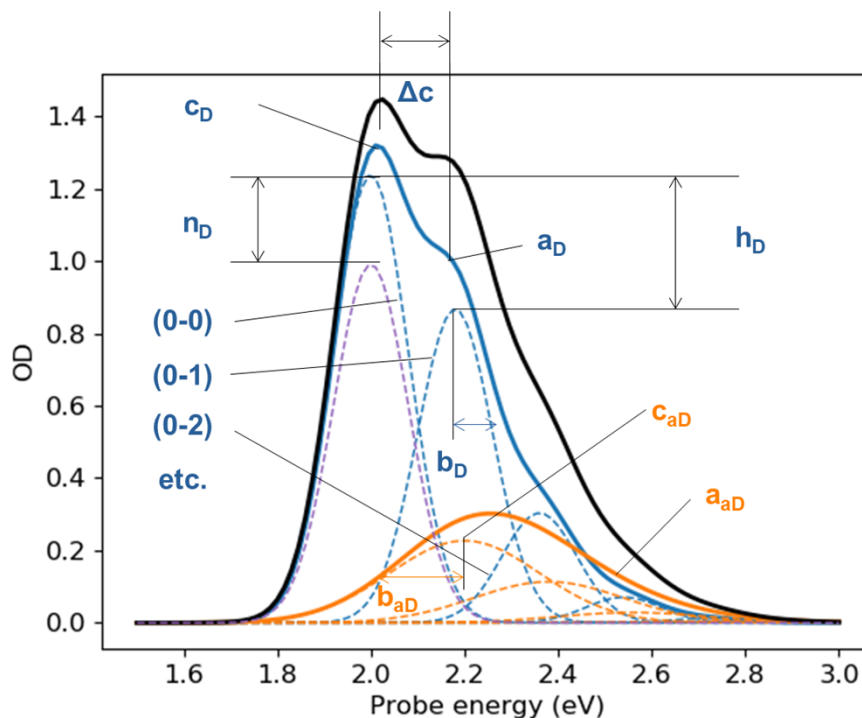


Figure S7. Spectral decomposition of the lowest energetic optical absorption of the donor polymer (suffix “D”) in the solid state into contributions from the ordered (blue) and amorphous phase (orange, suffix “a”). The decomposed spectra are further decomposed into vibronic contributions, according to Spano’s model [Refs. 23, 24a (main manuscript)],

assuming a single essential vibronic progression (dashed lines). For a donor-acceptor blend, the same analysis is done for the lowest energetic acceptor absorption. As the relative height of the dashed lines and their energetic spacing are both given by a single parameter (h_D and Δc , respectively), the model accommodates significant spectral overlap between donor and acceptor absorption while still yielding reasonable uncertainties for the phase specific morphological parameters

List of spectral features and their relation to morphological parameters

Name [unit]	Provenience	Meaning	Morphology relation
$a_{D/A}$ [eV]	Fit parameter	Total area under blue curve	Persistence length, anisotropy, film thickness
$b_{D/A}$ [eV]	Fit parameter	Gaussian bandwidth of each single blue dashed curve	Energetic disorder
$c_{D/A}$ [eV]	Fit parameter	Center energy of dashed curve for (0-0) vibronic transition	Domain size / dielectric coupling
$h_{D/A}$ []	Fit parameter	Huang-Rhys factor for single effective vibronic progression	Wavefunction delocalization (on-chain ordering)
$n_{D/A}$ []	Fit parameter	Relative suppression of (0-0) vibronic due to weak H aggregation according to Spano's model (fixed to 0.5)	Weak H aggregates (on- chain ordering)
Δc [eV]	Fit parameter	Effective single vibronic progression (fixed to 0.185 eV)	Vibronic coupling
a_{tot} [eV]	$a_D + a_{aD} + a_A$	Total area under black curve (donor + acceptor)	Film thickness, anisotropy
A_{tot} [eV]	$a_A + a_{aA}$	Total area under black curve (only acceptor)	Total amount of acceptor
D_{tot} [eV]	$a_D + a_{aD}$	Total area under black curve (only acceptor)	Total amount of donor
X_A []	A_{tot}/a_{tot}	Relative spectral weight of acceptor in lowest energetic	D:A ratio

		optical transition	
X_{amD} []	a_{aD}/D_{tot}	Relative spectral weight of amorphous phase in donor absorption	Order, domain size
X_{amA} []	a_{aA}/A_{tot}	Relative spectral weight of amorphous phase in acceptor absorption	Order, domain size

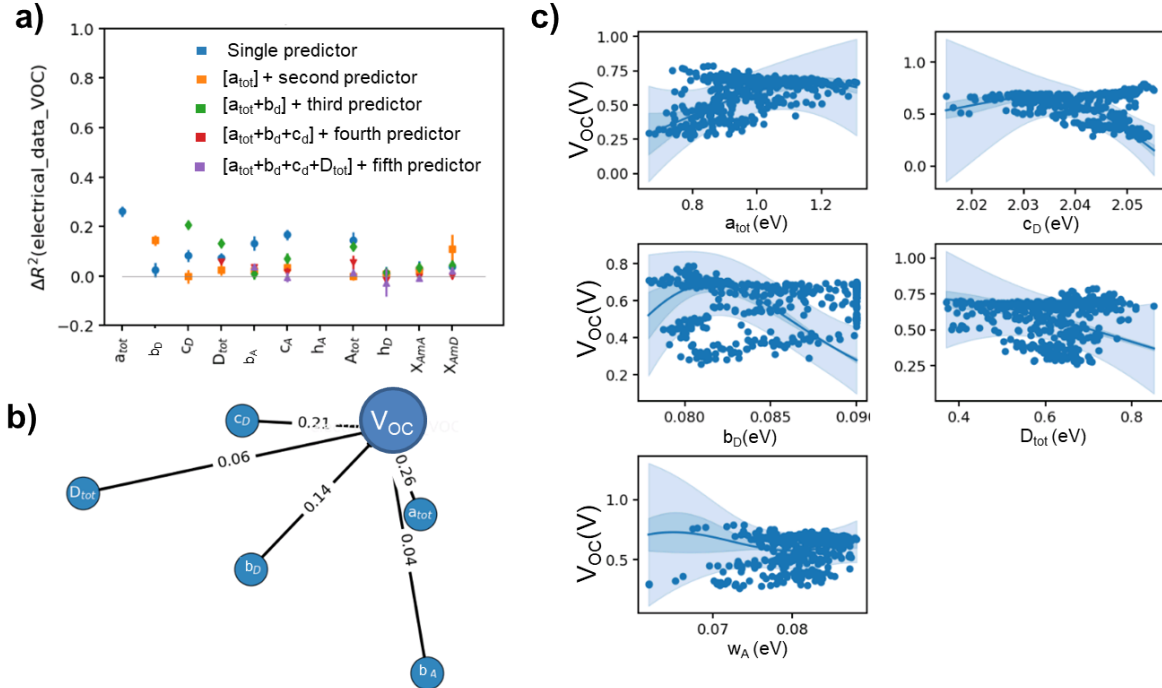


Figure S8: Prediction of V_{OC} from active layer morphology by minimum Redundancy Maximum Relevance embedded Gaussian Process Regression (mRMR-GPR). a) results mRMR-GPR runs: single predictor (blue symbols); two predictors including best blue predictor (orange); three predictors including best blue and best orange predictor (green), four predictors (red), five predictors (purple). b) differential explanation of variance by each selected predictor. Explanation values below 10% are considered irrelevant. The predictors are arranged in a spring model according to their explanation of variance c) one-dimensional intersections through the approximate objective function for V_{OC} , as obtained by mRMR-GPR (blue solid line), light blue and dark blue areas: 95% confidence intervals for the uncertainty of a single prediction and uncertainty of the mean, respectively.

Figure S8a shows the working principle of the minimum Redundancy Maximum Relevance (mRMR) embedded feature extraction using GPR [Ref. 22 (main manuscript)]. First, V_{OC} is predicted using only single predictors one by one (blue symbols). Several features are able to explain around 20% of the variance in the measured V_{OC} values. Next, the strongest single predictor (a_{tot}) is retained and a second predictor is included from the remaining predictor list (orange symbols). Comparing the orange symbols with the blue ones, we find for most of the predictors (see e.g. b_A , c_A) that they do not provide additional explanation of variance once a_{tot} is considered. However, there are two examples (b_D and X_{amD}) where the explanation of variance increases under the presence of a_{tot} (orange symbol has higher value than blue

symbol). This points to a non-linear correlation between \mathbf{b}_D and V_{OC} which was only found once the main correlation of \mathbf{a}_{tot} was included in the feature list. Again, the stronger of these two predictors (\mathbf{b}_D) is included into the feature list, and the procedure is repeated (green symbols) until a maximum number of allowed features is reached (5 in this work).

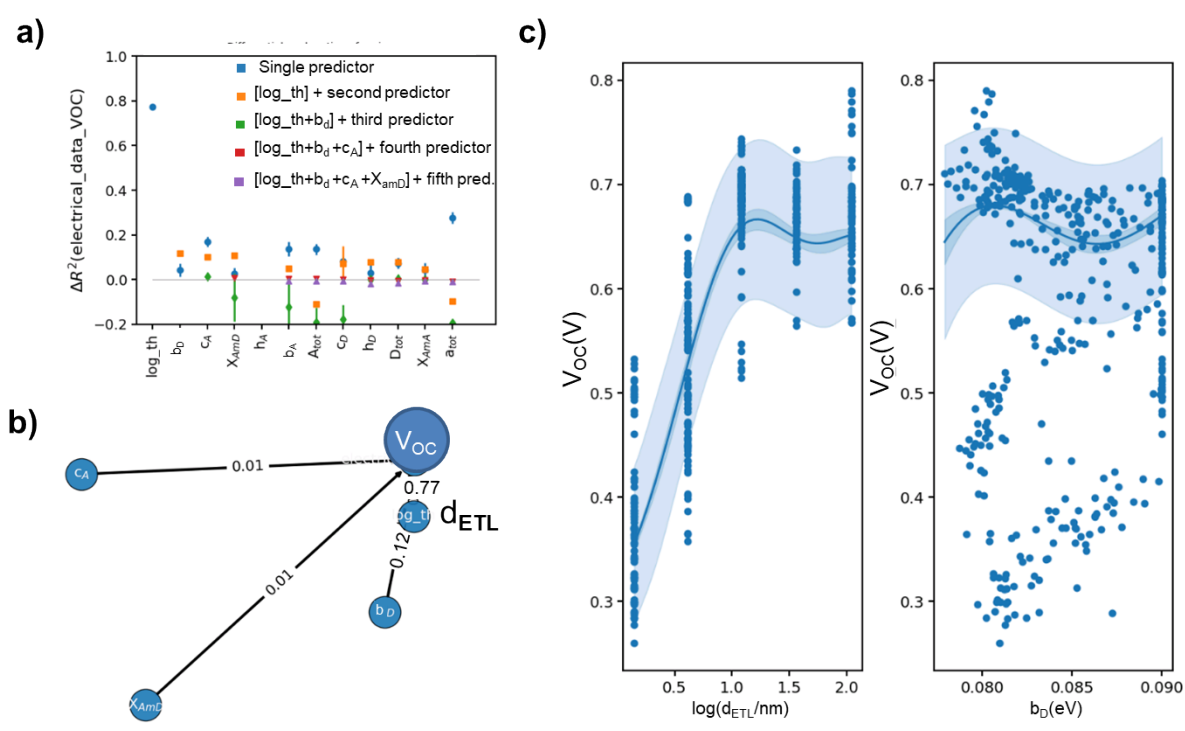


Figure S9: Prediction of V_{OC} from active layer morphology and d_{ETL} by mRMR-GPR. a) results of mRMR-GPR runs clearly showing that d_{ETL} is more important for V_{OC} than AL morphology: as a single predictor (blue), a_{tot} explains 25% of the variance, as shown in Figure S2a. But as soon as d_{ETL} (given as logarithmic value named \log_th) is included into GPR (orange), a_{tot} provides no additional explanation of variance, compare blue symbol with symbols of other colors at position “ a_{tot} ”, b) explanation of variance by selected predictors, c) one-dimensional intersections through the approximate objective function for V_{OC} , as obtained by mRMR-GPR (blue solid line), light blue and dark blue areas: 95% confidence intervals for the uncertainty of a single prediction and uncertainty of the mean, respectively.

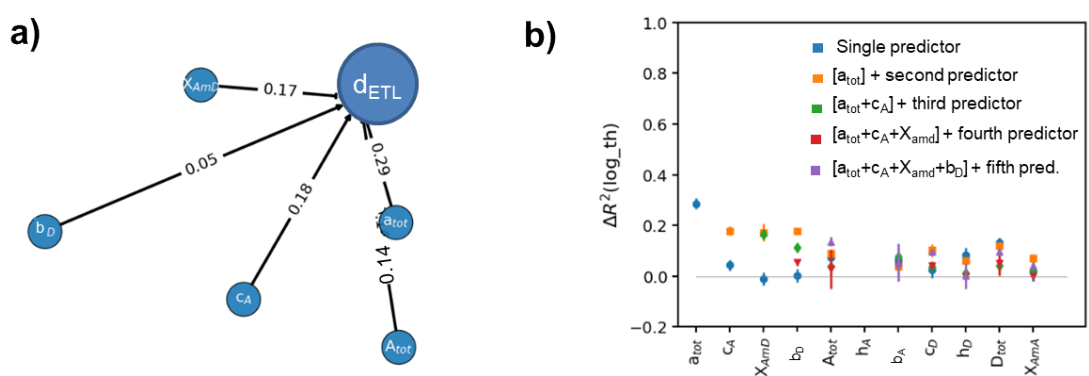


Figure S10: Prediction of d_{ETL} from active layer morphology by mRMR-GPR. a) Differential explanation of variance by selected predictors, b) mRMR – GPR procedure.

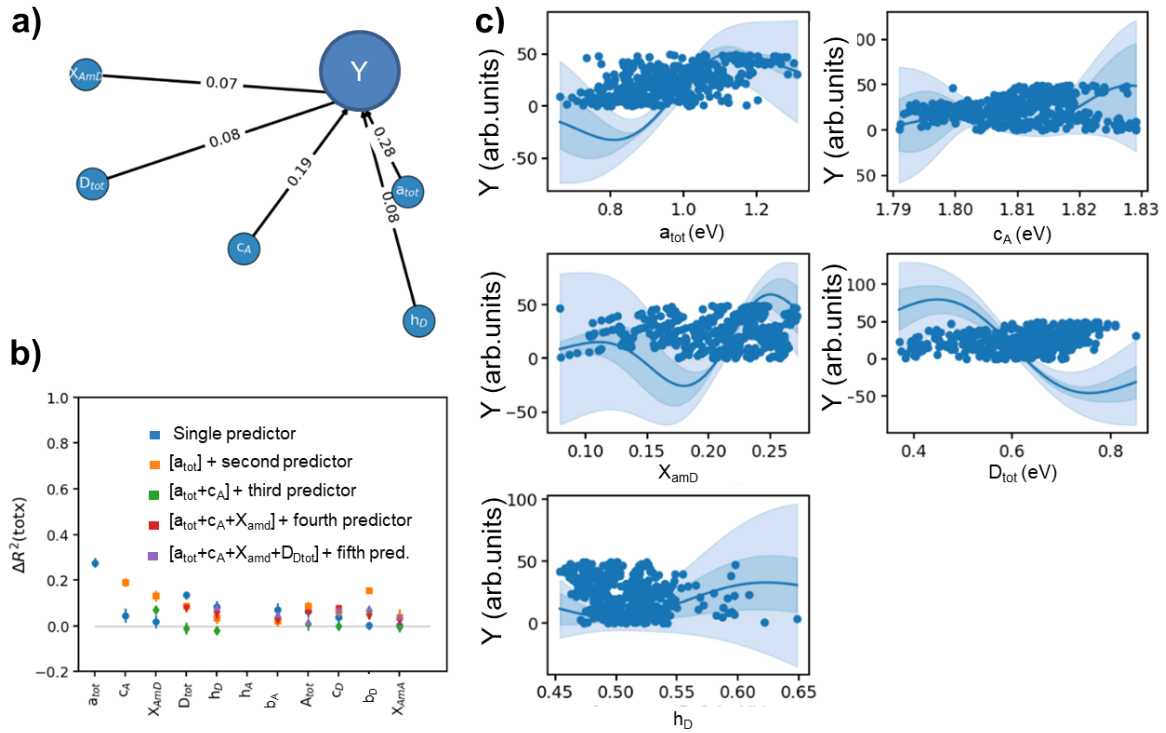


Figure S11: Prediction of the cross-web position Y from active layer morphology by mRMR-GPR. a) Differential explanation of variance by selected predictors, b) results of mRMR – GPR procedure. c) One-dimensional intersections through the approximate objective function for V_{OC} , as found by GPR (blue solid line), light blue and dark blue areas: 95% confidence intervals for the uncertainty of a single prediction and uncertainty of the mean, respectively.

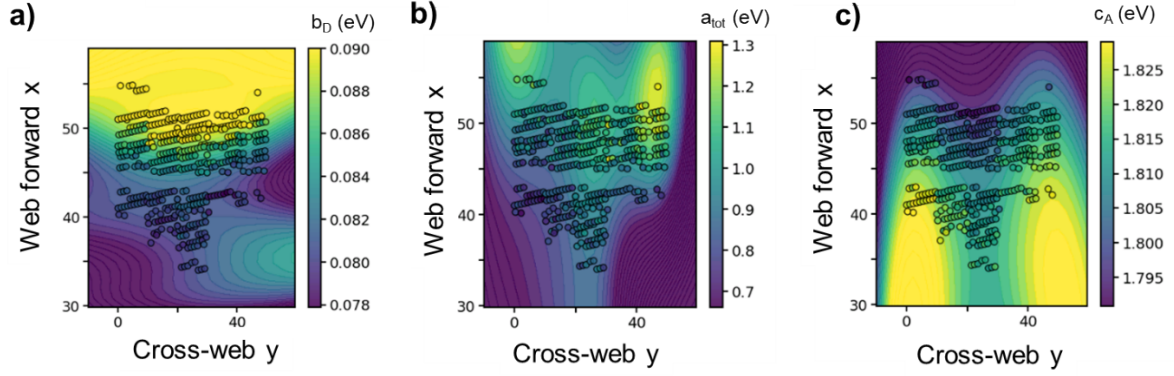


Figure S12: Evolution of active layer morphology across (y) and along (x) the web direction. a) Donor exciton bandwidth, b) total exciton absorption (donor + acceptor), c) acceptor exciton energy.

Figure S12 shows the evolution of active layer morphology across (y) and along (x) the web direction. We find that the donor bandwidth (panel a) shows a variation nearly exclusively along x, where the D:A ratio is varied. Hence, in acceptor-rich blends ($x > 50$, corresponding to $w_A \cong 0.7 - 0.75$), we find that donor bandwidth is high, which may point to an increase of disorder in the donor phase. From this observation, in Fig. 5d in the main text we draw causal links from x to w_A , and from w_A to b_D , but we draw no arrow from y to b_D .

In contrast, the total exciton absorption a_{tot} is mainly influenced along the cross-web direction y, see Fig. S12b. The total absorption, and hence the film thickness, is especially high for $y > 40$, which is the region of the thinnest ETL stripe. This explains the high correlation between ETL thickness and a_{tot} , found in Fig. S8a; therefore, in the knowledge graph in Fig. 5d, we can draw a causal connection from y to an unknown processing condition P_{AL} acting on AL, and from P_{AL} to a_{tot} . We can speculate that P_{AL} is given by an unequal distribution of nozzle flow rates.

Finally, the acceptor exciton energy c_A is influenced by both x and y, see Fig. S12c. A lower exciton energy means extended J aggregates. Along the web forward direction, we find that the exciton energy decreases for acceptor-rich blends, which makes sense because domains will be the larger the less disturbed by the polymer donor. However, we also see a symmetric evolution of c_A along the cross-web direction y, meaning that the exciton energy is higher at the edges than in the center. This means that at constant X_A , in the center larger acceptor domains are formed than in the edges, which may come from a small temperature gradient over the annealing mat, being slightly colder in the edges.

6. Optimal processing parameters

In order to find the uncertainty of the optimal processing parameters, we perform a brute force sampling of the two-dimensional objective function displayed in Fig. 5c), to encounter the data range where $u_{cb} \geq \max(\text{PCE})$, where u_{cb} is the upper confidence bound for PCE with respect to the uncertainty of the mean. We find $X_{A,i} = 0.59 \pm 0.04$; and $d_{ETL} = 17 \pm 4$ nm.

7. Drift-Diffusion Simulations

The drift-diffusion simulations were performed using the open-source program SIMSalabim version 4.45.[1, Ref. 25 in main manuscript]

SIMSalabim solves the 1D drift-diffusion equations which consist of a set of three main equations, the Poisson, continuity and drift-diffusion equations.

The Poisson equation:

$$\frac{\partial}{\partial x} \left(\varepsilon(x) \frac{\partial V}{\partial x} \right) = -q (p(x) - n(x) + C_i(x))$$

where x is the position in the device,¹ q the electric charge, V the electrostatic potential, n and p the electron and hole concentrations, and ε the permittivity. C_i can represent any other type of charges in the systems such as: (i) doping with N_A^- and N_D^+ being the ionized p-type and n-type doping respectively, or (ii) the charged traps Σ_T^+ and Σ_T^- for hole and electron traps. Such as the Poisson equation may be written as:

$$\frac{\partial}{\partial x} \left(\varepsilon \frac{\partial V}{\partial x} \right) = -q (p - n + N_D^- - N_A^+ + \Sigma_T^+ - \Sigma_T^-)$$

The current continuity equations:

¹ Note that for notation convenience the x dependence of the variables will be dropped in the following. However, in a multilayer stack not only densities values are meant to vary with x but also values such as mobilities and dielectric constant.

$$\frac{\partial J_n}{\partial x} = -q(G - R)$$

$$\frac{\partial J_p}{\partial x} = q(G - R)$$

with $J_{n,p}$ the electron and hole currents, G and R the generation and recombination rate respectively.

The movement of these free charges is governed either by diffusion due to a gradient in carrier density or by drift following the electric field such as the electron and hole currents can be written as:

$$J_n = -q n \mu_n \frac{\partial V}{\partial x} + q D_n \frac{\partial n}{\partial x}$$

$$J_p = -q p \mu_p \frac{\partial V}{\partial x} - q D_p \frac{\partial p}{\partial x}$$

with $\mu_{n,p}$ the charge carrier mobilities and $D_{n,p}$ carrier diffusion coefficients. The carrier diffusion coefficients can be written following Einstein's equation such as:

$$D_i = \frac{k_B T}{q} \mu_i$$

with k_B the Boltzmann's constant, T the absolute temperature.

For the simulation, we chose to place the cathode at $x = 0$ and the anode at $x = L$ as a convention, L being the total thickness of the device.

In order to numerically solve the system of equations presented above we need to specify the boundary conditions for the carrier densities:

$$n(0) = N_c \exp\left(-q \frac{\varphi_n}{k_B T}\right) \quad \dots \quad n(L) = N_c \exp\left(-q \frac{E_g - \varphi_n}{k_B T}\right)$$

$$p(0) = N_v \exp\left(-q \frac{E_g - \varphi_p}{k_B T}\right) \quad \dots \quad p(L) = N_v \exp\left(-q \frac{\varphi_p}{k_B T}\right)$$

and the potential at the contacts:

$$q (V(L) - V(0) + V_{app}) = W_c - W_a$$

with N_c and N_v the effective density of states for the conduction and valence band respectively, here we chose N_c and N_v to be equal, φ_n and φ_p the electron and hole injection barrier at the cathode and anode, V_{app} being the externally applied voltage and W_a and W_c the anode and cathode work functions respectively.

The recombination rate R is typically expressed by adding the contribution from the band-to-band/bimolecular recombination and Shockley-Read-Hall (SRH) recombination from equations:

$$R_B = \gamma(np - n_i^2)$$

$$R_{SRH} = \frac{C_n C_p \Sigma_T}{C_n(n + n_1) + C_p(p + p_1)} (np - n_i^2)$$

γ is the bimolecular recombination rate constant, n_i is the intrinsic carrier concentration, n_1 and p_1 are constants that depend on the trap energy level (E_{trap}), and C_n and C_p are the capture coefficients for electrons and holes respectively. n_1 and p_1 are defined as followed:

$$n_1 = N_c \exp\left(-q \frac{E_c - E_{trap}}{k_B T}\right)$$

$$p_1 = N_v \exp\left(-q \frac{E_{trap} - E_v}{k_B T}\right)$$

For more information about how this system of equations is solved we encourage the readers to read references [2,3,4].

Table S1: Device parameters used to simulate the devices. The varied parameters values for each donor:acceptor combination and the different SnO₂ thicknesses can be found in Figures S10a-f. Note that for simplicity and to remove some parameters to optimize for the fits the PEDOT:PSS/AgNW is set as an effective electrode forming an ohmic contact with the active layer and with a work function W_a .

Parameter	Unit	Value
P3HT:o-IDTBR		
E_c / E_v	eV	3.6 / 4.8
N_c	m ⁻³	2×10^{27}
L	nm	100
ϵ_r	-	3.5
μ_p	m ² V ⁻¹ s ⁻¹	2.52×10^{-8}
μ_n	m ² V ⁻¹ s ⁻¹	Varied
G_{ehp}	m ⁻³ s ⁻¹	Varied
γ	m ³ s ⁻¹	Varied
Σ_T	m ⁻³	Varied
E_{trap}	eV	4.21
C_n / C_p	m ³ s ⁻¹	10^{-13}
SnO₂		
E_c / E_v	eV	Varied / 8.18
N_c	m ⁻³	3.63×10^{24}
L	nm	4.1 – 12.2 – 36.6
ϵ_r	-	10
S_T (SnO ₂ Interface)	m ⁻²	Varied
Electrode Work functions		
W_a	eV	4.8
(PEDOT:PSS/AgNW)		
W_c	eV	Aligned to the SnO ₂ E_c
(IMI)		
External Parameters		
R_s	Ω m ²	Varied
R_{sh}	Ω m ²	Varied

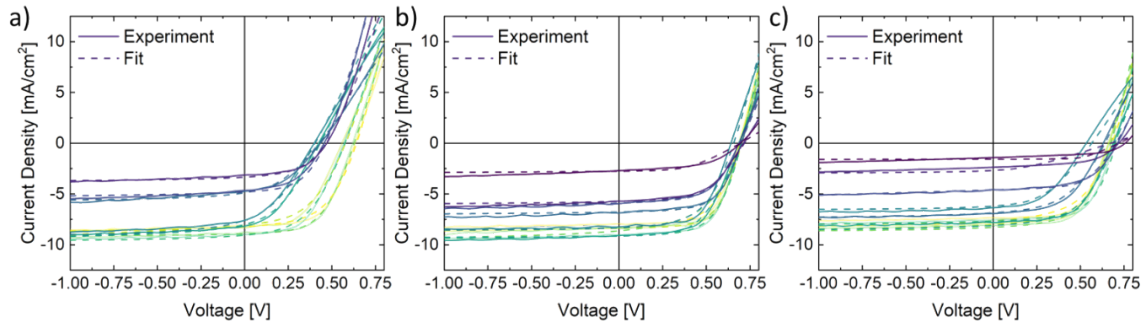


Figure S13: Fitting results for the different donor:acceptor ratios for the different SnO₂ thicknesses: a) 4.1 nm b) 12.1 nm and c) 36.6 nm

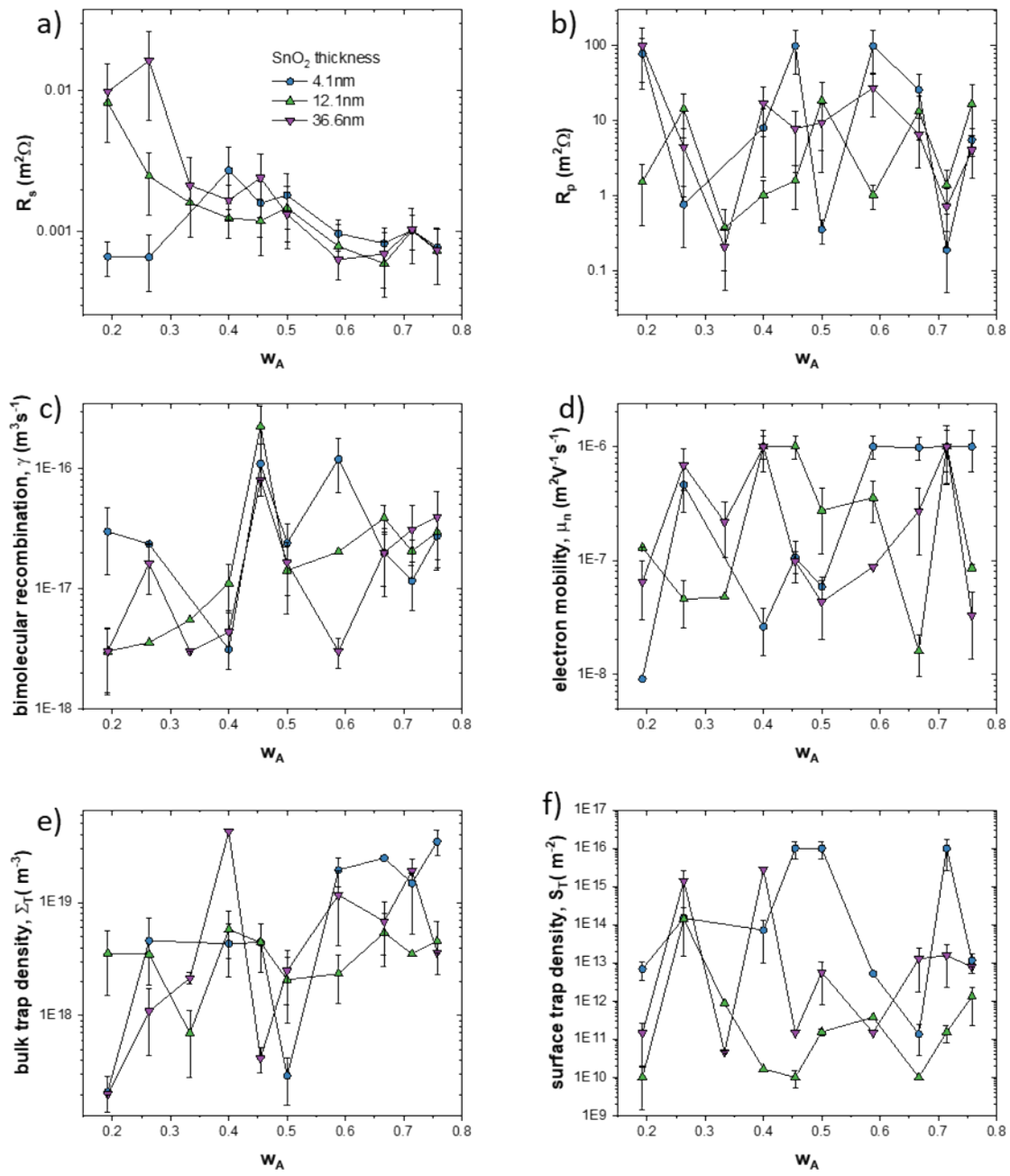


Figure S14: Additional parameters obtained from drift-diffusion fitting, plotted against the acceptor mass fraction w_A and for different ETL thicknesses (blue: 4.1nm, green: 12.1nm, violet: 36.6 nm, as given in panel a). a) series resistance R_s , b) parallel resistance R_p , c) bimolecular recombination coefficient γ , d) electron mobility μ_n , e) bulk trap density Σ_T , f) surface trap density S_T . None of these parameters show a clear dependence on the acceptor fraction or the ETL thickness.

8. Fitting procedure with Bayesian optimization

Our fitting procedure is based on the bayesian optimization package from scikit-optimize[<https://scikit-optimize.github.io/stable/>] using the skopt.Optimizer framework.

The skopt.Optimizer is used to minimize the mean-square error (MSE) between the experimental data and the simulated data with SIMsalabim by optimizing the value of the different material parameters described in table S1. Figure S15 describes the logic behind the optimization procedure. In our case, the experimental data is the 1 sun JV curve for each device and the physical model is the drift-diffusion model described in the previous section. The cost function to minimize is the MSE and we used a gaussian process regressor (GPR) as a surrogate model (we also tested other surrogates but the GPR performed the best). To ensure a good balance between exploration and exploitation of the entire parameter space we used the ‘gp_hedge’ option for the acquisition function. We performed a random initial sampling (80 points) using the Latin hypercube algorithm followed by 200 points of bayesian optimization distributed over 4 cores.

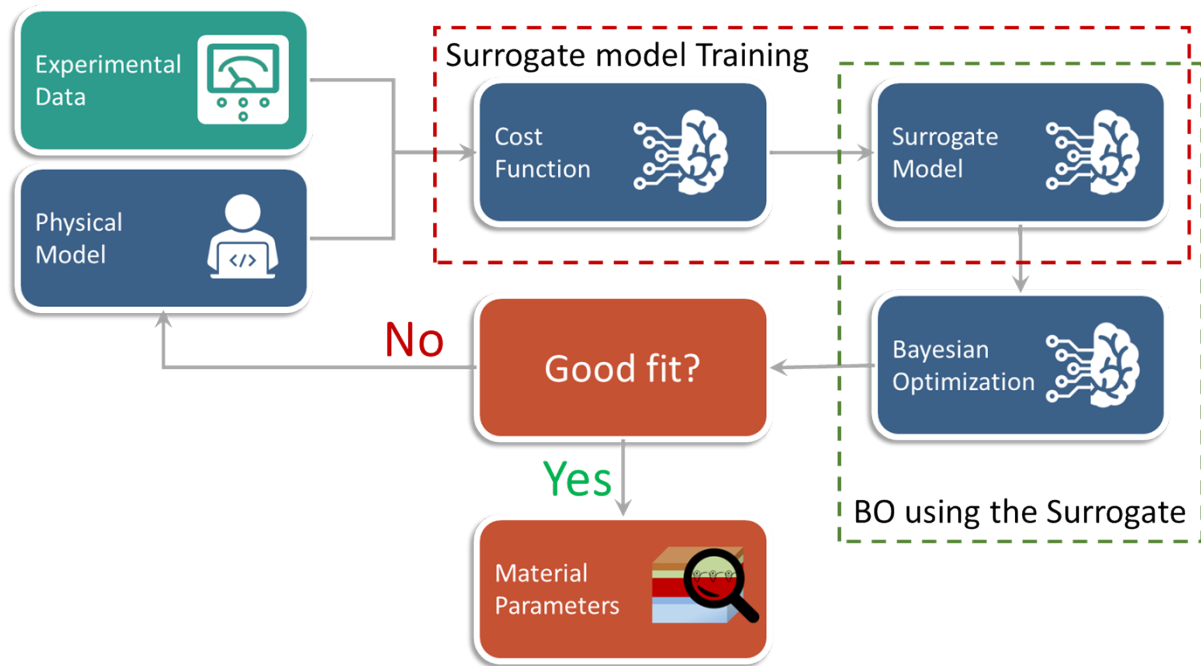


Figure S15: Flowchart describing the optimization procedure to perform the JV-curve fitting procedure using Bayesian optimization.

References

- [1] Koopmans et al., (2022). SIMsalabim: An open-source drift-diffusion simulator for semiconductor devices. *Journal of Open Source Software*, 7(70), 3727, <https://doi.org/10.21105/joss.03727>
- [2] Selberherr, S., *Analysis and Simulation of Semiconductor Devices*, Springer (1984)
- [3] Koster, L.J.A., Smits, E.C.P., Mihailetschi, V.D., Blom, P.W.M., Device model for the operation of polymer/fullerene bulk heterojunction solar cells, *Phys. Rev. B* **72**, 085205 (2005)
- [4] Koopmans, M., Koster, L.J.A., Voltage Deficit in Wide Bandgap Perovskite Solar Cells: The Role of Traps, Band Energies, and Effective Density of States, *Solar RRL* **6**, 2200560 (2022)